Effects of surfactant solubility on the hydrodynamics of a viscous drop in a dc electric field

Herve Nganguia, Wei-Fan Hu, Ming-Chih Lai, and Y.-N. Young

Phys. Rev. Fluids **6**, 064004 — Published 29 June 2021

DOI: 10.1103/PhysRevFluids.6.064004

Effects of Surfactant Solubility on the Hydrodynamics of a Viscous Drop in a DC Electric Field

Herve Nganguia[1], Wei-Fan Hu[2], Ming-Chih Lai[3] and Y.-N. Young[4*]

[1]*Department of Mathematics, Towson University, Towson, MD 21286, USA*

[2]*Department of Mathematics, National Central University,*

300, Zhongda Road, Taoyuan 32001, Taiwan

[3]*Department of Applied Mathematics,*

National Chiao Tung University, 1001,

Ta Hsueh Road, Hsinchu 30050, Taiwan

[4]*Department of Mathematical Sciences,*

New Jersey Institute of Technology, Newark, NJ 07102, USA

(Dated: June 14, 2021)

Abstract

Surfactants (amphiphilic surface active agents) are often used to control the dynamics of viscous drops and bubbles in microfluidics applications. Surfactant sorption kinetics has been shown to play a critical role in the deformation of drops in extensional and shear flows, yet to the best of our knowledge these kinetics effects on a viscous drop in an electric field have not been accounted for. In this paper we numerically investigate the effects of sorption kinetics on a surfactant-covered viscous drop in an electric field. Over a range of electric conductivity and permittivity ratios between the interior and exterior fluids, we focus on the dependence of deformation and flow on the transfer parameter J, and Biot number Bi that characterize the extent of surfactant exchange between the drop surface and the bulk. Our findings suggest solubility affects the electrohydrodynamics of a viscous drop in distinct ways as we identify parameter regions where (1) surfactant solubility alters both the drop deformation and circulation of fluid around a drop, and (2) surfactant solubility affects mainly the flow and not the deformation.

* Corresponding author: Y.-N. Young (yyoung@njit.edu)

I. INTRODUCTION

Electric field is widely utilized to deform a viscous drop in microfluidics and many petroleum engineering applications. Electrohydrodynamics (EHD), generally referred to as the motion of fluid induced by an electric field, is highly relevant to transport and manipulation of small liquid drops in microfluidic devices. Over the past two decades, dielectrophoresis, electro-osmosis, and induced-charge electro-osmosis in EHD have deeply influenced the field of microfluidics. Moreover, the integration of EHD into microfluidic-based platforms has led to the development of technological platforms for manipulation of particles, colloids, droplets, and biological molecules across different length scales [1–6]. EHD has been used in a wide range of applications, such as spray atomization, fluid motion of bubble drop, electrostatic spinning, and printing [1, 7–12]. In material and bioengineering, EHD was utilized to manufacture nanostructured materials [13, 14] and manipulate charged macromolecules [15].

For a leaky dielectric drop freely suspended in another leaky dielectric fluid, the bulk charge neutralizes on a fast timescale while "free" charges accumulate on (and move along) the drop surface. In this physical regime, the full electrokinetic transport model in a viscous solvent can be described by a charge-diffusion model that can be further reduced to derive the Taylor-Melcher (TM) leaky dielectric model [16]. In many physics and engineering applications with moderately dissolvable electrolytes, the TM leaky dielectric model can capture the deformation of a viscous drop in both dielectric medium [17, 18] and a conducting medium [19, 20]. The TM model has been extended in recent years to include the effects of charge relaxation [21], charge convection [22–25], and the investigation of non-spherical drop shapes [26–29] and drop instabilities using direct numerical methods [30–36].

In the absence of surface-active agent (surfactant), the balance between the electric stresses and the hydrodynamic stress on the drop surface gives rise to a drop shape and a flow field that can be parametrized by the conductivity ratio and the permittivity ratio [37]. Under a small electric field, a steady equilibrium drop shape exists due to the balance between the electric and hydrodynamic stresses [34, 38, 39]. For a sufficiently large electric field, instabilities arise and the drop keeps deforming until it eventually breaks up into smaller drops [40, 41].

Non-ionic surfactant has been extensively used for stability control in experiments on

TABLE I. Summary of published modeling work on the electrohydrodynamics (EHD) of a surfactant-laden viscous drop. SM denotes the small deformation (spherical harmonics) analysis, and LD refers to the large deformation (spheroidal harmonics) analysis. The abbreviations LS-RegM, BIM, and IIM stand for level-set regularized method, boundary integral method, and immersed interface method, respectively. Inertia-driven flow (Navier-Stokes) is shortened using N.-S.

Fluids	Electric field	Surfactants	Method	References
Stokes	dc, uniform	insoluble	analytical (SD)	[42]
N.-S.	dc, uniform	insoluble	numerical (LS-RegM)	[43]
Stokes	dc, uniform	insoluble	(semi-) analytical (LD)	[44, 45]
Stokes	dc, uniform	insoluble	numerical (BIM)	[46, 47]
Stokes	dc, uniform	insoluble	analytical & numerical	[48–50]
Stokes	dc, nonuniform	insoluble	analytical & numerical	[51]
Stokes	dc, uniform	**soluble**	numerical (IIM)	Present Work

electrodeformation of a viscous drop [42, 46, 52–54]. By reducing the surface tension and inducing a significant Marangoni stress due to the surfactant transport on the interface, surfactant could lead to drastically different EHD of a surfactant-laden viscous drop. Table I summarizes the existing theoretical and numerical investigations in the literature. In most of these studies [42–51, 55], surfactants are assumed to be insoluble and the surface tension is described using either a linear relationship, or more realistically the Langmuir equation of state

$$\gamma(\Gamma) = \gamma_0 + RT\Gamma_\infty \ln\left(1 - \frac{\Gamma}{\Gamma_\infty}\right), \tag{1}$$

where R and T denote the gas constant and absolute temperature, respectively. γ_0 is the surface tension of an otherwise clean drop, and Γ_∞ is the maximum surface packing limit. A spheroidal model has been developed to predict the large electro-deformation of a viscous drop covered with insoluble surfactant [44]. Finite surfactant surface diffusivity has also been incorporated in such spheroidal model [45] with excellent agreement with full numerical simulations [47].

Studies have shown that sorption kinetics and interactions between surfactants molecules

can be effectively used to alter the concentration of surfactants at the drop interface [56–59], and have profound effects on the drop shape and dynamics [60–65]. Electric field can in turn affect the rate of sorption kinetics [55]. These results naturally lead to the following inquiries: *What effects does adsorption and/or desorption have on EHD and how do they affect the interplay between all the various stresses?* To our knowledge these questions have yet to be addressed in the literature.

In this work we aim to fill the gap by numerically solving the coupled equations for the leaky-dielectric model and surfactant transport equations. While our method is general enough to handle interaction between surfactants molecules, here we assume the relation provided by the Langmuir equation of state Eq. 1 to focus on the effects of surfactants solubility. In the present study, we investigate such dynamics in hopes of elucidating the physics governing the EHD of drops in the presence of soluble surfactants.

The paper is organized as follows: In §II, we present the physical problem and formulate the governing equations. In §III we investigate how solubility affects the stability of various drop shapes by systematically exploring a range of electric parameters across the $(\sigma_r, \varepsilon_r)$ phase diagram. Then, in §IV, we investigate the effects of the transfer parameter J, a measure of the strength of surfactant exchange between drop surface and bulk. In §V, we end our study with a summary of how surfactants solubility affects deformation for surfactant-covered drops in electric fields.

II. THEORETICAL MODELING

We consider a viscous drop immersed in a leaky dielectric fluid in the presence of surfactants and subject to an electric field, as shown in figure 1. Each fluid is characterized by the fluid viscosity μ, dielectric permittivity ε, and conductivity σ with the superscript denoting interior (-) or exterior (+) fluid. In this work we denote the contrasts of those properties by $\mu_r = \mu^+/\mu^-$, $\varepsilon_r = \varepsilon^-/\varepsilon^+$, and $\sigma_r = \sigma^+/\sigma^-$. Following [41], note the inverse convention for the permittivity ratio. Moreover, in this work $\mu^+ = \mu^-$.

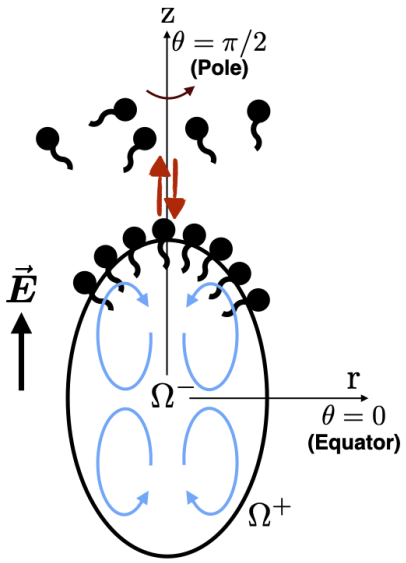

FIG. 1. Sketch of the problem: A leaky dielectric viscous drop (Ω^-) immersed in another dielectric fluid (Ω^+), with an external electric field $\vec{\mathbf{E}}$ in the z direction. The bead-rod particles represent surfactants at the interface or in the bulk. The double arrows denote adsorption-desorption kinetics while the curved arrows represent the induced flow. The curved arrow across the vertical axis shows the symmetry around the z-axis. The equator and pole are represented by the angle parameter $\theta = 0$ and $\theta = \pi/2$, respectively.

A. Formulation

The fluids are governed by the incompressible Stokes equations, neglecting inertia

$$-\nabla p + \mu \nabla^2 \boldsymbol{u} = \mathbf{0}, \tag{2}$$

where p and $\boldsymbol{u}$ are the pressure and velocity field, respectively. The electric field $\mathbf{E} = -\nabla\phi$, where ϕ is the electric potential that satisfies the Laplace equation both inside and outside the drop in the extended leaky dielectric model,

$$\nabla^2 \phi = 0. \tag{3}$$

The surfactant transport on the drop surface and in the exterior bulk fluid are described by the following set of coupled equations

$$\frac{\partial \Gamma}{\partial t} + \nabla_s \cdot (\Gamma \boldsymbol{v}_s) + \Gamma(\nabla_s \cdot \boldsymbol{n})\boldsymbol{u}_s \cdot \boldsymbol{n} = D_s \nabla_s^2 \Gamma + \beta C_s \left(\Gamma_\infty - \Gamma\right) - \alpha \Gamma, \tag{4}$$

$$\frac{\partial C}{\partial t} + \boldsymbol{u} \cdot \nabla C = D \nabla^2 C, \tag{5}$$

where $\boldsymbol{n}$ is the normal vector, $\boldsymbol{u}_s$ is the surface velocity on the drop and $\boldsymbol{v}_s = (\mathbf{I} - \boldsymbol{n}\boldsymbol{n})\boldsymbol{u}_s$ is the velocity tangential component along the drop ($\mathbf{I}$ is the identity tensor). Γ and C are the surfactant concentration on the drop surface and in the bulk outside the drop, respectively; C_s is the concentration of surfactant in the fluid immediately adjacent to the drop surface; α and β are the kinetic constants for desorption and adsorption, respectively; D_s and D are the diffusion constant on the drop surface and in the bulk correspondingly.

At the drop interface, boundary conditions are imposed for the electric potential ϕ, the flow field $\boldsymbol{u}$, and the bulk surfactant concentration C. First, the electric potential is continuous and the total current is conserved,

$$[\![\phi]\!] = 0, \quad \underbrace{[\![\sigma \nabla \phi \cdot \boldsymbol{n}]\!]}_{\text{Ohmic current}} = \underbrace{\frac{d\tilde{q}}{dt}}_{\text{Charge relaxation}} + \underbrace{\nabla_s \cdot (\tilde{q}\boldsymbol{u}_s)}_{\text{Charge convection}}, \tag{6}$$

where $\tilde{q} = -[\![\varepsilon \nabla \phi \cdot \boldsymbol{n}]\!]$ represents the surface charge density, and $[\![\cdot]\!]$ denotes the jump between outside and inside quantities. The effects of charge relaxation on the transient behavior of drop [21], and of convection on equilibrium deformation [22, 25, 66], have been investigated analytically and numerically in the context of drops electrohydrodynamics. In the present study, we neglect these effects to more easily isolate the surfactant effects. This reduces Eq. 6 to:

$$[\![\phi]\!] = 0, \quad [\![\sigma \nabla \phi \cdot \boldsymbol{n}]\!] = 0. \tag{7}$$

Second, the electric and fluid problems are coupled through the stress balance

$$\underbrace{[\![-p + \mu\left(\nabla \boldsymbol{u}^T + \nabla \boldsymbol{u}\right)]\!]}_{\text{Hydrodynamic stress}} \cdot \boldsymbol{n} + \underbrace{[\![\varepsilon\left(\boldsymbol{E}\boldsymbol{E} - \frac{1}{2}(\boldsymbol{E}\cdot\boldsymbol{E})\mathbf{I}\right)]\!]}_{\text{Electric stress}} \cdot \boldsymbol{n} = \underbrace{\gamma(\nabla_s \cdot \boldsymbol{n})\boldsymbol{n}}_{\text{Surface tension}} - \underbrace{\nabla_s \gamma}_{\text{Marangoni stress}}. \tag{8}$$

Surfactants act to lower the surface tension, which now depends on the concentration of surfactants through the equation of state Eq. 1. As a result, the non-uniform surfactant distribution induced by the flow in and around the drop yields a surface tension gradient (the Marangoni stress).

Finally, to close the system we need a third boundary condition that describes the flux of surfactants between the surface of the drop and the bulk. The interfacial condition for the surfactant concentration,

$$D\boldsymbol{n}\cdot\nabla C=\beta C_s\left(\Gamma_\infty-\Gamma\right)-\alpha\Gamma, \tag{9}$$

where $\boldsymbol{n}\cdot\nabla C = \partial C/\partial\boldsymbol{n}$ denotes the normal derivative of C: Positive values denote adsorption-dominated surfactant kinetics, whereas negative values denote desorption-dominated surfactant kinetics. We henceforth concentrate on axisymmetric solutions only.

B. Nondimensionalization

We use the drop size r_0 to scale length, capillary pressure γ_0/r_0 to scale pressure, equilibrium surfactant concentration Γ_{eq} to scale Γ, initial surfactant concentration C_0 to scale the bulk surfactant concentration, and electrically driven flow $U_d=\varepsilon^+E_0^2r_0/\mu$ to scale velocity, in which E_0 denotes the intensity of the external electric field. Note that in the presence of soluble surfactant, Γ_{eq} denotes the equilibrium with the bulk surfactant C_0 [67], whereas for the insoluble case Γ_{eq} is the initial uniform surfactant concentration.

There are nine independent dimensionless physical parameters that characterize this system: (1) the electric capillary number $\mathrm{Ca}_E\equiv\mu U_d/\gamma_{eq}=\varepsilon^+E_0^2r_0/\gamma_{eq}$ (ratio of electric pressure to capillary pressure), (2) permittivity ratio $\varepsilon_r=\varepsilon^-/\varepsilon^+$, (3) conductivity ratio $\sigma_r=\sigma^+/\sigma^-$, (4) the elasticity constant $E=RT\Gamma_\infty/\gamma_0$ in the Langmuir equation of state, (5) the surfactant coverage $\chi=\Gamma_{eq}/\Gamma_\infty$, (6) the surface surfactant Péclet number $\mathrm{Pe}_s=r_0U_d/D_s$, (7) the bulk surfactant Péclet number $\mathrm{Pe}=r_0U_d/D$, (8) the transfer parameter $J=C_0D/\Gamma_{eq}U_d$ and (9) the Biot number $\mathrm{Bi}=\alpha\tau_{EHD}$ (ratio of EHD characteristic time scale $\tau_{EHD}=r_0/U_d$ to desorption time scale).

The elasticity number E measures the sensitivity of the surface tension to the surface surfactant concentration, whereas in the presence of surfactant exchange between the bulk and the drop interface, the surfactant coverage is related to the adsorption constant $k=\beta C_0/\alpha$ in Eq. 10 [56, 57]

$$\chi=\frac{k}{k+1}. \tag{10}$$

Note that for the insoluble case, the surfactant coverage $\chi=\Gamma_{eq}/\Gamma_\infty$ results from scaling the surfactant concentration in Eq. 1. The bulk and surface Péclet numbers denote the

relative strength of convective transport versus diffusive transport. These two numbers also represent the ratio of two time scales: $\mathrm{Pe} = \tau_D/\tau_{EHD}$, where $\tau_D = r_0^2/D$ is the surfactant diffusion time scale. The parameter J gives a measure of transfer of surfactant between its bulk and adsorbed forms relative to advection on the interface. It is important to note the ratio Bi/J distinguishes two types of transport regime [68, 69]: diffusion-controlled transport ($\mathrm{Bi}/J > 1$), and sorption-controlled transport ($\mathrm{Bi}/J \ll 1$). Moreover the bulk Péclet number and the transfer parameter are related by $J = 1/h_{\mathrm{ad}}\mathrm{Pe}$, where h_{ad} is the adsorption depth that measures the extent of surface dilution due to surfactant adsorption. In terms of the above dimensionless parameters, the clean drop cases correspond to $E = 0$ or $\chi = 0$ (Eq. 15). The case of insoluble surfactants corresponds to $\mathrm{Bi} = 0$ (Eq. 16c). The non-diffusive case corresponds to $\mathrm{Pe}, \mathrm{Pe}_s \gg 1$.

We obtain the following dimensionless equations

$$-\nabla p + \mathrm{Ca}\nabla^2 \boldsymbol{u} = \boldsymbol{0}, \tag{11}$$

$$\nabla^2 \phi = 0, \tag{12}$$

$$\frac{\partial \Gamma}{\partial t} + \nabla_s \cdot (\Gamma \boldsymbol{v}_s) + (\nabla_s \cdot \boldsymbol{n})\boldsymbol{u}_s \cdot \boldsymbol{n}\Gamma = \frac{1}{\mathrm{Pe}_s}\nabla_s^2 \Gamma + J\boldsymbol{n} \cdot \nabla C, \tag{13}$$

$$\frac{\partial C}{\partial t} + \boldsymbol{v} \cdot \nabla C = \frac{1}{\mathrm{Pe}}\nabla^2 C, \tag{14}$$

$$\gamma = 1 + E\ln(1 - \chi\Gamma) \tag{15}$$

where $\mathrm{Ca} = [1+E\ln(1-\chi)]\mathrm{Ca}_E$. On the drop surface, the dimensionless boundary conditions are given by

$$[\![\phi]\!] = 0, \quad [\![\sigma\nabla\phi \cdot \boldsymbol{n}]\!] = 0, \tag{16a}$$

$$[\![-p + \mathrm{Ca}\left(\nabla \boldsymbol{u}^T + \nabla \boldsymbol{u}\right)]\!] \cdot \boldsymbol{n} + [\![\mathrm{Ca}_E \left(\boldsymbol{E}\boldsymbol{E} - \frac{1}{2}(\boldsymbol{E} \cdot \boldsymbol{E})\mathbf{I}\right)]\!] \cdot \boldsymbol{n} = \gamma(\nabla_s \cdot \boldsymbol{n})\boldsymbol{n} - \nabla_s \gamma, \tag{16b}$$

$$J\boldsymbol{n} \cdot \nabla C = \mathrm{Bi}\left[C_s\left(1 + k - k\Gamma\right) - \Gamma\right]. \tag{16c}$$

In Eq.11 and Eq. 16b the capillary number $\mathrm{Ca} = \mu U_d/\gamma_0$ is the ratio of electric stress to tension in the absence of surfactant.

The right-hand side of the stress balance Eq. 16b shows that two surfactant-related mechanisms govern the deformation of drops. The first mechanism is driven by the capillary pressure, and acts in the normal direction. It is further broken down into two phenomena: tip-stretching and surface dilution [70]. In tip-stretching, a decrease in surface tension $\gamma < 1$

at the pole due to surfactant yields *larger* drop deformation compared with the surfactant-free case. The area-average surface tension γ_{avg} gives a global measure of the dilution effect: compared with the clean case, *smaller* deformations are attained for $\gamma_{\text{avg}} > 1$. The second mechanism is driven by the Marangoni stress, which acts to suppress [70, 71] or even reverse [71] surface convective fluxes. The Marangoni stress acts in the tangential directions, and consists of two principal components: the derivative of surface tension as a function of surfactant concentration ($\partial\gamma/\partial\Gamma$) and the surfactant concentration gradient ($\partial\Gamma/\partial\theta$), where θ is the angle parameter.

These nontrivial and highly nonlinear mechanisms pose challenges in studying the EHD of a surfactant-laden viscous drop. Analytical solutions of the transport equation are only possible in very restricted limits [72], and often numerical simulations are necessary. Several computational methods have been developed to simulate surfactants effects on droplets [73–76]. In the context of EHD, we refer the readers to the results in [43, 46, 77].

In this work we implement a numerical code based on the immersed interface method (IIM) integrating numerical tools developed by our group [35, 78, 79]. A description of the numerical setup is provided in appendix A, together with numerical validation in appendix B and convergence study in appendix C.

Moreover we fix the elasticity constant $E = 0.2$ and conduct simulations with various combinations of parameters to investigate the effects of surfactant solubility on the drop electrohydrodynamics. Our simulations show that deformation and flow patterns appear to be invariant with increasing surfactant solubility when the surfactant coverage $\chi < 0.8$. We therefore focus our analysis on elevated surfactant coverage with $\chi = 0.9$. This surfactant coverage is in the relevant range in many experimental setups [42, 67, 80], and the corresponding (dimensionless) surface tension $\gamma_{eq} = 1 + E\ln(1-\chi) = 0.54$ and adsorption number $k = \chi/(1-\chi) = 9$. The Péclet numbers $\text{Pe} = \text{Pe}_S = 100$ in §III. It is then increased to $\text{Pe} = \text{Pe}_S = 500$ for the prolate shapes in § IV. The transfer parameter $J = 10^{-2}$ for the oblate cases, and $J = 2\times10^{-3}$ for the prolate cases. These values of the bulk Péclet number and transfer parameter yield an adsorption depth $h_{\text{ad}} = 1$, which is physically relevant for a millimeter size drop with $\Gamma_\infty = 2.5\times10^{-6}$ m^2/mol and bulk surfactant concentration ten times the critical micelle concentration (CMC) [67]. The limit $J \ll 1$ corresponds to the diffusion-controlled surfactant transport that is relevant in many practical applications [69]. At $T = 0$, the drop is spherical, and the surfactant concentrations $C = 1$ and $\Gamma = 1$ are

imposed uniformly in the bulk and on the drop surface, respectively.

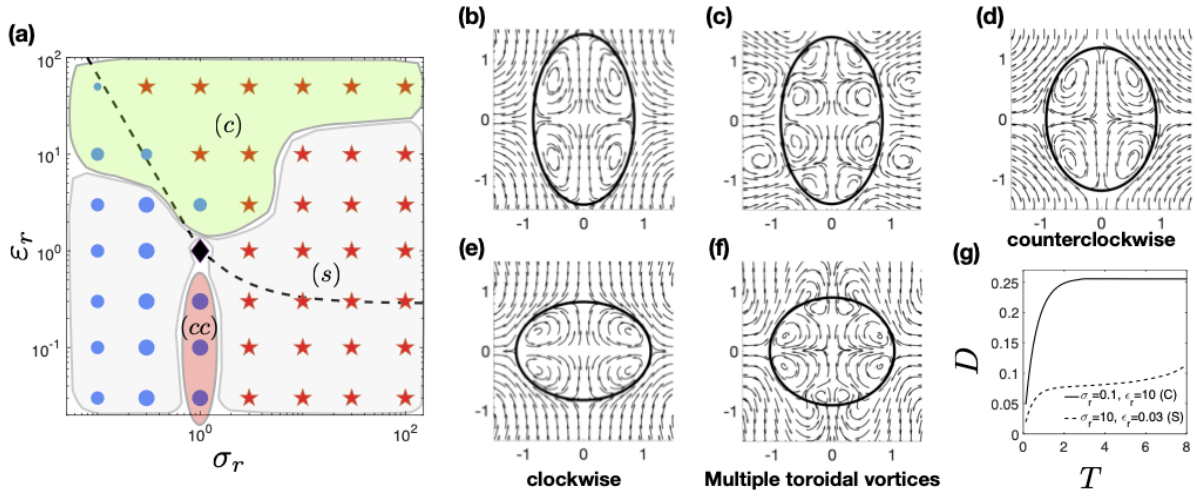

FIG. 2. (a): Phase diagram for the insoluble case (Biot number $\mathrm{Bi} = 0$) with surfactant coverage $\chi = \Gamma_{eq}/\Gamma_\infty = 0.9$ and $\mathrm{Pe}_S = 100$. (b-d): prolate drops with three types of circulation. (e,f): oblate drops with two types of circulation. (g): Drop deformation versus time. One drop with $(\sigma_r, \varepsilon_r) = (0.1, 10)$ reaches a steady equilibrium (solid line), while the drop with $(\sigma_r, \varepsilon_r) = (10, 0.03)$ continues to elongate (dashed line) past $T = 10$. In each panel, the vector fields are plotted on a relative scale.

III. GENERAL SURFACTANT EFFECTS ON A VISCOUS DROP UNDER AN ELECTRIC FIELD

The shape of a clean viscous drop under an electric field can be either prolate, oblate or spherical with either a clockwise or counterclockwise circulation. The circulation is counterclockwise when $\varepsilon_+/\sigma_+ > \varepsilon_-/\sigma_-$, and clockwise otherwise [81]. The dashed line in figure 2a represents Taylor's discriminating function and delimits between prolate and oblate shapes. The circulation pattern, counterclockwise (equator-to-pole) or clockwise (pole-to-equator), are determined according to the flow inside the first quadrant of a axisymmetric drop in our numerical setup (figure 14b; also see [41] and references therein). A steady equilibrium drop shape exists as long as the electric capillary number Ca_E is below the critical value. Beyond this value the viscous drop continues to elongate and eventually breaks up with complicated flow patterns inside the drop [41].

A. Insoluble surfactant: Bi = 0

When covered with insoluble surfactants (negligible adsorption-desorption kinetics), we find that insoluble surfactants may give rise to multiple toroidal vortices in a spheroidal drop, which is not observed for a clean drop [41]. This is summarized in figure 2, which shows that due to an insoluble surfactant a prolate drop can have a clockwise circulation [panel (b)], multiple toroidal vortices in a quadrant [panel (c)] and a counter-clockwise circulation [panel (d)]. Panel (f) shows that the flow inside an oblate drop can also have multiple toroidal vortices in a quadrant. In addition to changing the flow pattern, we also find that surfactants can reduce the critical capillary number to below $\mathrm{Ca}_E = 0.3$ as shown in panel G, where a drop with multiple toroidal vortices continues to elongate past $T = 10$ at $\mathrm{Ca}_E = 0.3$. Consequently the deformation number, defined as $D = \frac{L-B}{L+B}$ (L is the length of the major axis and B is the length of the minor axis of the ellipsoid), continues to increase (dashed curve) in this case.

Figure 2(a) is the phase diagram of a surfactant-laden viscous drop with $\chi = 0.9$ and $\mathrm{Bi} = 0$ (no adsorption-desorption kinetics). For each point we simulate the electrohydrodynamics up to $T = 10$ for several values of the electric capillary number up to $\mathrm{Ca}_E = 0.3$. A blue circle denotes that a steady equilibrium is reached before $T = 10$ and the critical capillary number is larger than 0.3. A red star denotes that a steady spheroidal drop shape is not stable and the critical capillary number is less than 0.3. The dashed curve in figure 2(a) separates an oblate drop (above the curve) from a prolate drop (below the curve). The shaded regions delimit the various circulation patterns: clockwise (c), counter-clockwise (cc), multiple toroidal vortices (s). Our numerical findings show that these circulation patterns are qualitatively similar for the range of electric capillary numbers we investigated ($\mathrm{Ca}_E \leq 0.3$).

The stability of spheroidal drop shape summarized in figure 2(a) is consistent with prediction from our previous semi-analytical model [45], which shows that equilibrium shapes exist below Taylor's discriminating function (prolate) with $\sigma_r \leq 1$: In these cases, the capillary pressure is greater than the normal component of the Maxwell stress (or electric pressure). The stability of a spheroidal drop is lost and equilibrium shapes cease to exist for drops below Taylor's discriminating function with $\sigma_r > 1$, where the electric pressure is greater compared to the capillary pressure.

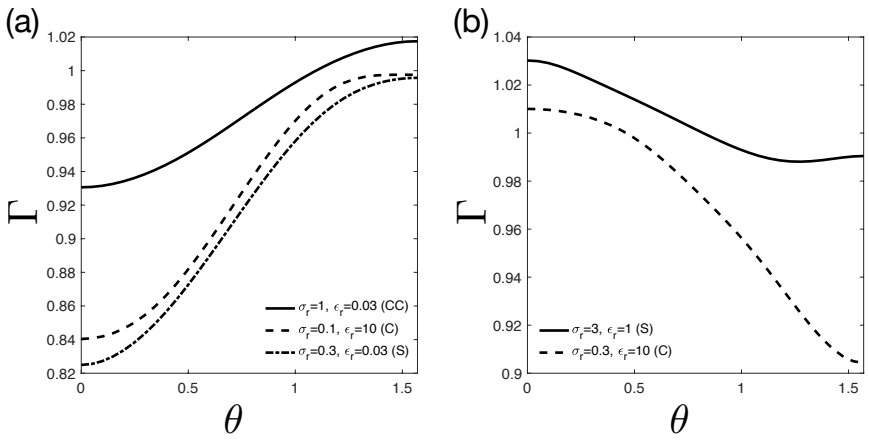

FIG. 3. (a) Surfactant distribution for the three prolate drops in figure 2(b,c&d). (b) Surfactant distribution for the two oblate drops in figure 2(e&f). The values $\theta = 0$ and $\theta = \pi/2$ denote the equator and pole, respectively.

Figure 3(a) shows the equilibrium surfactant distribution for the three prolate drops in figure 2, and (b) is the corresponding surfactant distribution for the two oblate drops in figure 2. We observe that regardless of the different flow patterns inside a drop, the surfactant concentration Γ is always maximum at the pole at $\theta = \pi/2$ for a prolate drop, while for an oblate drop Γ reaches maximum at the equator at $\theta = 0$. This is because at large Péclet number (low surfactant diffusivity) the dynamic surfactant redistribution from the initial homogeneous coverage is dominated by the surface dilation/contraction as the drop deforms. When the drop shape reaches an equilibrium, the surfactants also quickly approach a distribution that is close to the equilibrium distribution [70]: For a prolate (oblate) drop, the interface's contraction took place at the pole (equator) and hence the maximum surfactant at $\theta = \pi/2$ ($\theta = 0$).

For the prolate drops in figure 3(a), figure 4 shows the corresponding tangential velocity $u_t = \boldsymbol{v}_s \cdot \boldsymbol{t}$ [panel (a)], Marangoni stress $\gamma_s = -E\chi\Gamma_s/(1-\chi\Gamma)$ [panel (b)], normal Maxwell stress [panel (c)], and tangential Maxwell stress [panel (d)]. For the oblate drops in figure 3(b), figure 5 shows the corresponding tangential velocity u_t [panel (a)], Marangoni stress γ_s [panel (b)], normal Maxwell stress [panel (c)], and tangential Maxwell stress [panel (d)].

Combining the simulation results (such as those summarized in figures 3, 4 and 5) for all the cases in figure 2, we can draw the following conclusion: (1) The spatial distribution of the normal Maxwell stress correlates to the drop shape: Normal Maxwell stress is the largest

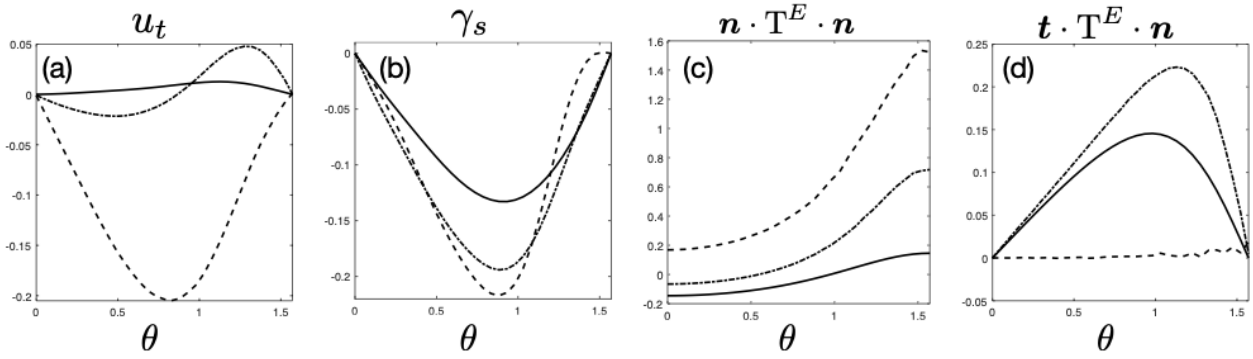

FIG. 4. For the three prolate drops in figure 2: (a) tangential velocity u_t, (b) Marangoni stress γ_s (the spatial derivative of surface tension γ), (c) normal Maxwell stress, and (d) tangential Maxwell stress. The values $\theta = 0$ and $\theta = \pi/2$ denote the equator and pole, respectively.

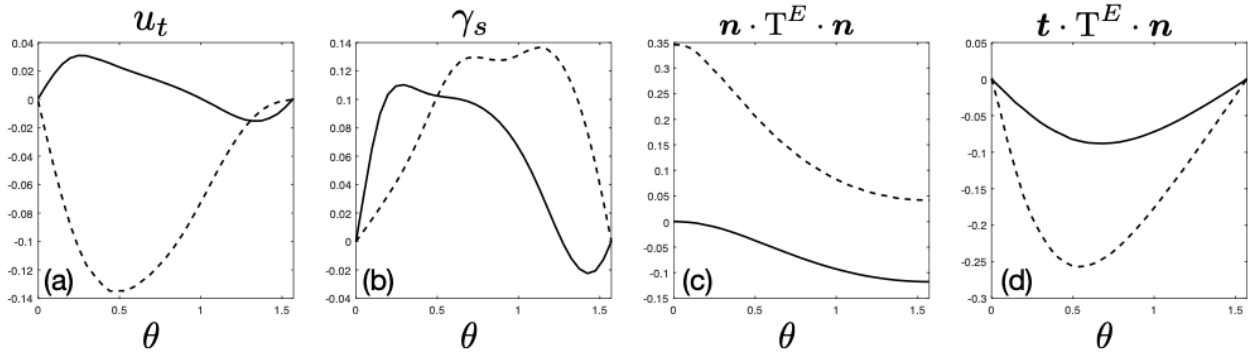

FIG. 5. For the two oblate drops in figure 2: (a) tangential velocity u_t, (b) Marangoni stress γ_s (the spatial derivative of surface tension γ), (c) normal Maxwell stress, and (d) tangential Maxwell stress. The values $\theta = 0$ and $\theta = \pi/2$ denote the equator and pole, respectively.

at the pole for a prolate drop, while for an oblate drop the normal Maxwell stress reaches maximum at the equator. (2) Similar to a clean drop, the flow magnitude in a clockwise circulation is larger than in a counter-clockwise circulation. The tangential Maxwell stress on a prolate drop with a clockwise circulation is nearly zero as in figure 4(c). This implies that, for a prolate drop with a clockwise circulation, the dominant balance in traction is between the viscous stress and the Marangoni stress. (3) For a prolate drop with a counter-clockwise circulation, the viscous stress is small and dominant balance in the traction is between the Maxwell stress and the Marangoni stress.

B. Soluble surfactant: Bi $= 10$ and $J = 10^{-2}$

In this section we investigate the effects of surfactant exchange on drop dynamics. To quantify these effects, we consider cases discussed in the previous section to clearly highlight how increasing the Biot number affects the dynamics. To draw direct comparison with the phase diagram in figure 2 for the insoluble cases, we summarize the results for the soluble cases in figure 6: Filled circles denote parameters where a steady spheroidal drop is found at equilibrium up to Ca $= 0.3$, while the stars are for parameters where the drop does not reach a steady spheroidal equilibrium for Ca $= 0.3$.

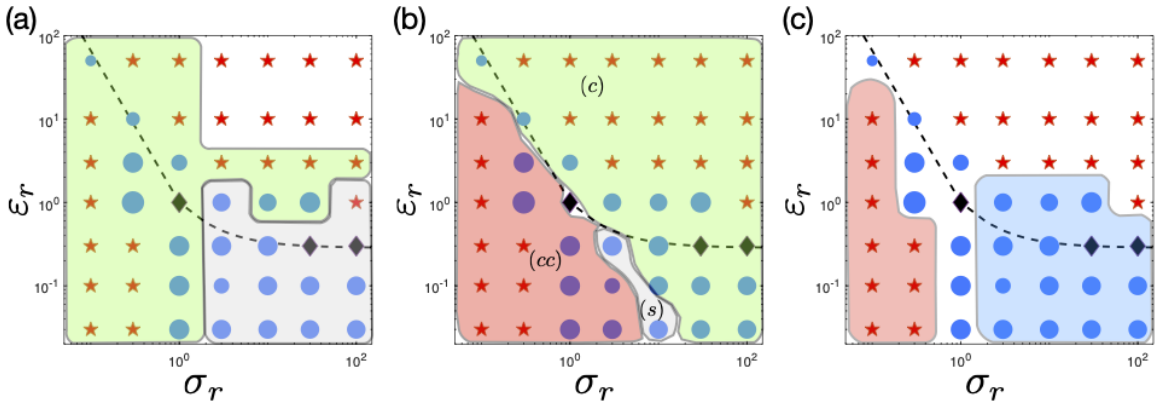

FIG. 6. Phase diagram for the soluble case (Biot number Bi $= 10$) with surfactant coverage $\chi = \Gamma_{eq}/\Gamma_\infty = 0.9$, $\mathrm{Pe}_S = 100$, and $J = 10^{-2}$. (a): The green-shaded region is for adsorption-dominance, and the gray-shaded region is for desorption-dominance. In the unshaded region, the relative change in the total amount of surface surfactant is small. (b): The clockwise (c), counter-clockwise (cc) and multiple toroidal vortices (s) circulation for a spheroidal equilibrium shape. (c): The red-shaded region denotes region in which solubility destabilizes the drop, and the blue-shaded region represents region in which solubility stabilizes the drop. The circle size denotes the relative change between a clean drop and a surfactant-covered drop.

Comparing between the insoluble results in figures 2 and the soluble results in figures 6 we find that surfactant solubility changes the steady equilibrium of a spheroidal drop: For parameters below the dashed curve in figure 2(a) and figure 6, we observe that surfactant solubility destabilizes the spheroidal drop for $\sigma_r < 1$, while stabilizes the spheroidal drop for $\sigma_r > 1$.

In figure 6(a) the green region represents parameters where the surfactant solubility leads to a net adsorption as the total amount of surfactant on the drop increases. The gray region

is for desorption-dominance, where the total amount of surfactant on the drop interfaces decreases. The sorption kinetics is minimal in the unshaded region in $\sigma_r > 3$, $\varepsilon_r > 3$, where the relative change in total surfactant concentration is less than 10^{-3}. Figure 6(b) shows the corresponding distribution of circulation patterns in the presence of soluble surfactants: The red region is for counter-clockwise (cc) circulation (equator to pole), the green region is for clockwise circulation (pole to equator), and the gray region is for multiple toroidal vortices inside the first quadrant of the drop.

Focusing on the parameters where the surfactant solubility alters the stability of a spheroidal drop, we find that in the adsorption-dominant region the stability is lost when the surfactant solubility decreases the average surface tension, as shown in the red region in figure 6(c). On the other hand, in the desorption-dominant region, the stability of a spheroidal drop is retained when the surfactant desorption leads to sufficient increase in average surface tension, as shown in the blue region in figure 6(c).

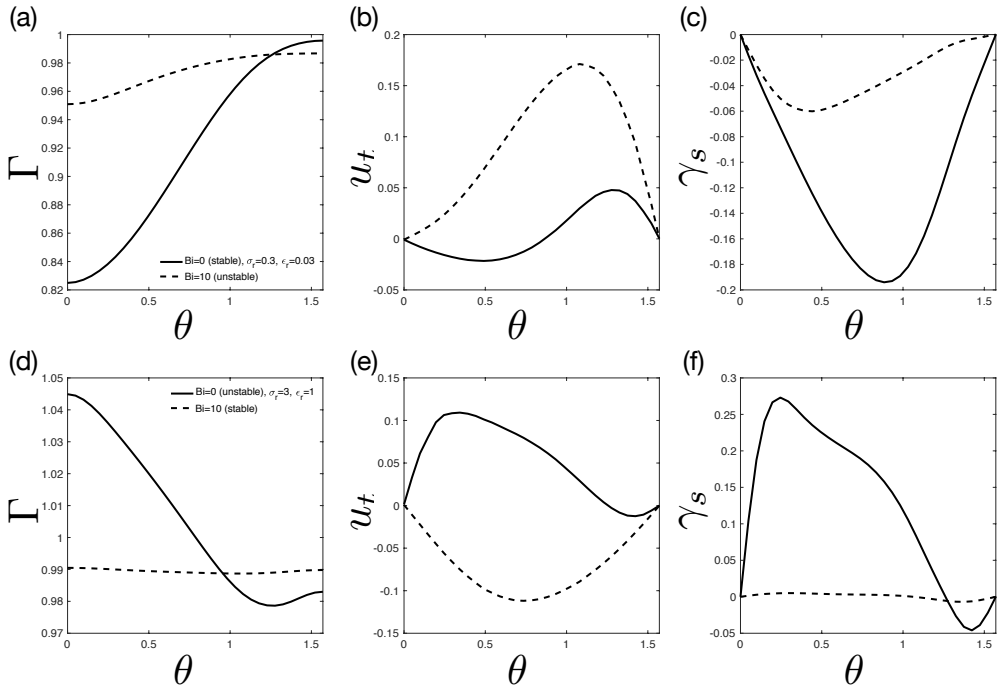

FIG. 7. Insoluble (solid line) versus soluble (dashed line) surfactants for a prolate drop (top row, $\mathrm{Ca}_E = 0.3$) and for an oblate drop (bottom row, $\mathrm{Ca}_E = 0.25$) on the (a,d) Surfactant distribution, (b,e) Tangential velocity $u_t = \boldsymbol{v}_s \cdot \boldsymbol{t}$, and (c,f) Marangoni stress γ_s (the spatial derivative of surface tension γ). The Péclet number $\mathrm{Pe} = 100$ and $J = 10^{-2}$, and the values $\theta = 0$ and $\theta = \pi/2$ denote the equator and pole, respectively.

Next we consider how surfactant sorption/desorption kinetics affects the drop dynamics at various combination of $(\sigma_r, \varepsilon_r)$: First we choose $(\sigma_r, \varepsilon_r) = (0.3, 0.03)$ as a representative case where a prolate drop can reach a steady equilibrium when $\mathrm{Bi} = 0$ (solid line in figure 7), and becomes unstable with $\mathrm{Bi} = 10$ (dashed line). Figure 7 illustrates the effect of solubility on surface distribution of surfactant (panels a&d), the tangential velocity u_t (panels b&d), and Marangoni stress γ_s (panels c&f). Adsorption onto the drop surface homogenizes the surfactant distribution (figure 7(a)), leading to smaller Marangoni stress (figure 7(c)) and stronger tangential flow (figure 7(b)). The Maxwell stress also sees an increase due to solubility, albeit small in comparison to the change in Marangoni stress. As surfactant exchange takes place, the capillary pressure is lowered and is overtaken by the electric pressure leading to a loss in stability.

For an oblate drop, we choose $(\sigma_r, \varepsilon_r) = (3, 1)$ as a representative case, where surfactant solubility stabilizes an oblate drop by piling up the drop surface with surfactant from the bulk. At this set of $(\sigma_r, \varepsilon_r)$, an oblate drop lacks an equilibrium spheroidal shape in the presence of insoluble surfactants (figure 2(a)). Increasing surfactant solubility suppresses the Marangoni stress almost entirely (figure 7(f)). The diminished Marangoni stress yields a clockwise circulation (figure 7(e)), identical to that observed for a clean spheroidal oblate drop. Put together, these results suggest solubility reestablishes the balance between viscous and Maxwell tractions leading to a steady spheroidal oblate drop.

For the remainder of our study, we investigate the effects of the transfer parameter J using values of the permittivity and conductivity ratios corresponding to existing data in the literature [38, 41, 43, 46, 51]. Comparison between figure 2(a) and figure 6(b) shows that the effects of solubility are much more pronounced for prolate drops. Thus in the following section we focus on the following three aspects of the solubility effects on a prolate drop: loss of stability, variability in the flow structure, and larger deformation with increasing surfactant exchange.

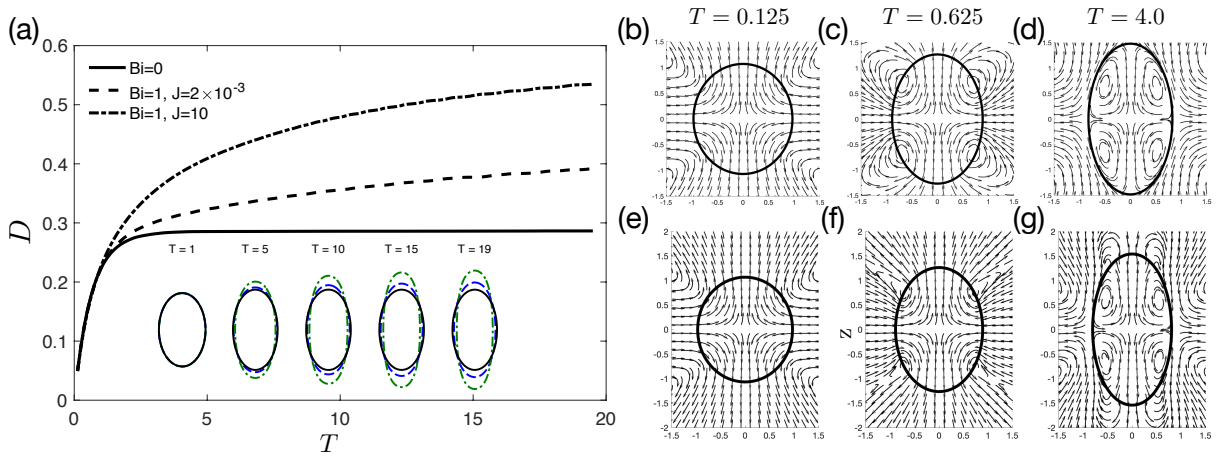

FIG. 8. (a) Deformation of a prolate drop with $(\sigma_r, \varepsilon_r) = (0.1, 5)$ as a function of dimensionless time T. The electric capillary number $\mathrm{Ca}_E = 0.25$. The Biot numbers $\mathrm{Bi} = 0$ (insoluble case) and $\mathrm{Bi} = 1$. The inset shows the drop shapes at various times. (b-d) Circulation for the prolate drop with $\mathrm{Bi} = 0$ at times $T = 0.125$, $T = 0.625$, and $T = 4$, respectively. (e-g) Circulation for the prolate drop with $\mathrm{Bi} = 1$ and $J = 2 \times 10^{-3}$ at times $T = 0.125$, $T = 0.625$, and $T = 4$, respectively. The Péclet number $\mathrm{Pe} = \mathrm{Pe}_S = 500$.

IV. EFFECTS OF SURFACTANT PHYSICO-CHEMISTRY ON A PROLATE DROP

A. Increasing Biot number destabilizes a prolate drop

Here we show that enhancing the surfactant solubility (by increasing Biot number) destabilizes a spheroidal prolate drop with $\sigma_r < 1$. We use the combination $(\sigma_r, \varepsilon_r) = (0.1, 5)$, where a surfactant-free viscous prolate drop has a counterclockwise circulation under an electric field. For a clean drop the steady equilibrium exists at all values of Ca_E [41]. For a drop covered with insoluble surfactants ($\mathrm{Bi} = 0$) and Péclet number $\mathrm{Pe}_S = 500$, we find that an equilibrium drop shape exists for $\mathrm{Ca}_E \leq 0.3$ (figure 2(a)): At $T = 0.125$ the drop first elongates along the electric field direction with a tangential flow on the interface that moves the surfactant from equator to pole (figure 8(b)). As the surfactant accumulates and builds up the Marangoni stress, a circulation from pole to equator develops around $T \sim 0.6$ (figure 8(c)) and the drop reaches an equilibrium prolate shape with a clockwise circulation after $T \sim 4$ (figure 8(d)). This circulation at equilibrium is opposite to that of a clean prolate 'A' drop with a much weaker flow strength.

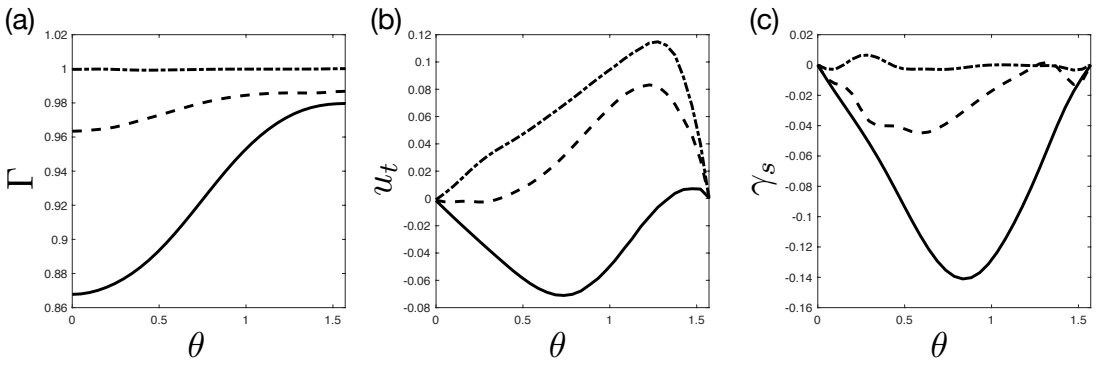

FIG. 9. Surfactant distribution (a), tangential velocity $u_t = \boldsymbol{v}_s \cdot \boldsymbol{t}$ (b), and Marangoni stress γ_s (the spatial derivative of surface tension γ) (c) for the prolate drop in figure 8 at $T = 19$. The solid lines are for $\mathrm{Bi} = 0$ (the insoluble surfactant case). The dashed and dash-dotted lines are for $\mathrm{Bi} = 1$ with $J = 2 \times 10^{-3}$ and $J = 10$, respectively. The Péclet number $\mathrm{Pe} = \mathrm{Pe}_S = 500$, and the values $\theta = 0$ and $\theta = \pi/2$ denote the equator and pole, respectively.

As we increase Bi (in the diffusion-controlled regime), we find that the steady spheroidal shape no longer exists and the drop keeps deforming until the end of simulations (up to $T = 20$), as illustrated by the dashed ($J = 2\times10^{-3}$) and dash-dotted ($J = 10$) lines in figure 8(a). For comparison, figure 8(e-g) shows the circulation with $\mathrm{Bi} = 1$ and $J = 2 \times 10^{-3}$ at times $T = 0.125, 0.625, 4$. Figure 9(c) shows that the Marangoni stress is reduced in magnitude because the surfactant on the drop surface is homogenized (figure 9(a)) by the adsorbed surfactants. Figure 9(b) shows the corresponding tangential velocity on the drop interface.

For insoluble surfactants [solid curves in figure 9(a&c)], the surfactant has the most spatial inhomogeneity that corresponds to a large Marangoni stress. With soluble surfactant in the diffusion-controlled regime ($\mathrm{Bi}/J > 1$, dashed curves) the surfactant sorption kinetics greatly reduces the Marangoni stress, giving rise to larger drop deformation. In the sorption-controlled regime ($\mathrm{Bi}/J = 0.1 < 1$, dash-dotted curves) the surfactant concentration Γ is nearly homogeneous and the Marangoni stress is quite small, corresponding to the largest and fastest deformation in figure 8. Moreover, with surfactants accumulating on the drop surface in equilibrium with the bulk, the capillary pressure is reduced below the electric pressure, leading to the loss of stability of a spheroidal prolate drop.

B. Effects of Biot number on flow around a prolate drop

Here we investigate the effects of solubility on the flow field. Specifically we focus on the combination $(\sigma_r, \varepsilon_r) = (1/3, 1)$ with $\mathrm{Ca}_E = 0.3$, where equilibrium prolate drop is found for both insoluble (figure 2) and soluble surfactants (figure 6). In the diffusion-controlled

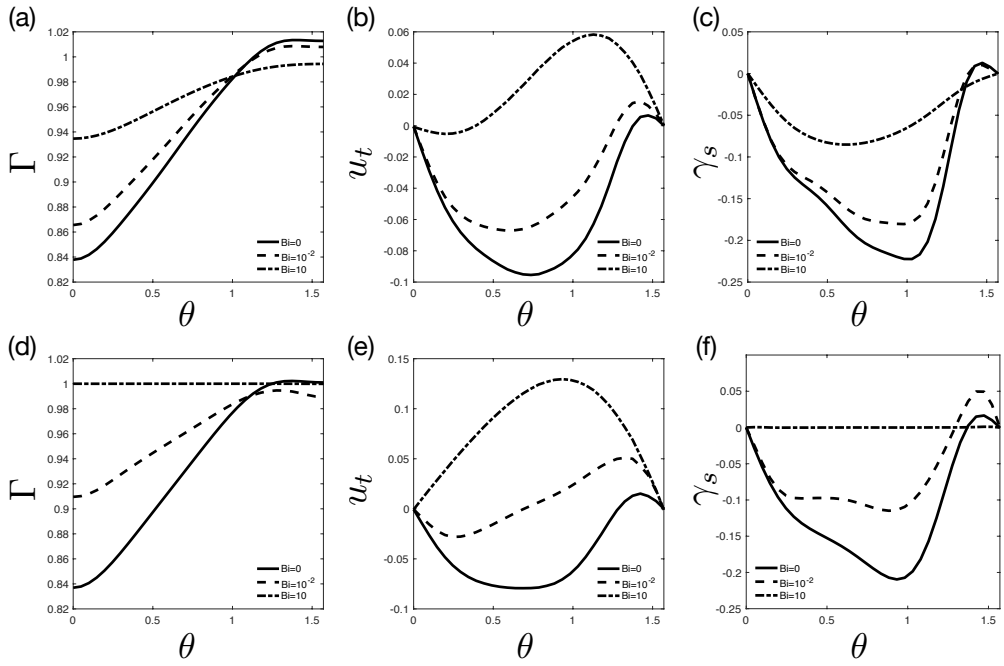

FIG. 10. A prolate drop with $(\sigma_r, \varepsilon_r) = (1/3, 1)$ and $\mathrm{Ca}_E = 0.3$. (a,d) Surfactant distribution, (b,e) tangential velocity $u_t = \boldsymbol{v}_s \cdot \boldsymbol{t}$, and (c,f) Marangoni stress γ_s (the spatial derivative of surface tension γ) as a function of θ. Solid lines are for $\mathrm{Bi} = 0$ (the insoluble surfactant case), dashed lines are for $\mathrm{Bi} = 10^{-2}$, and dash-dotted lines are for $\mathrm{Bi} = 10$. The transfer parameter $J = 2 \times 10^{-3}$ (a-c), and $J = 10$ (d-f). The Péclet number $\mathrm{Pe} = \mathrm{Pe}_S = 500$, and the values $\theta = 0$ and $\theta = \pi/2$ denote the equator and pole, respectively.

regime, simulations show that the equilibrium drop deformation is minimally influenced by surfactant solubility for $\mathrm{Ca}_E \in [0, 0.3]$ because sorption kinetics induce little change in the total amount of surfactant (figure 12(a)). Consequently the average surface tension does not vary much with Bi, leading to little change in drop deformation with increased surfactant solubility.

The flow pattern, on the other hand, is highly dependent on the surfactant distribution and kinetics. Without surfactant a clean equilibrium prolate drop with $(\sigma_r, \varepsilon_r) = (1/3, 1)$ has a counter-clockwise flow under an electric field. For $\mathrm{Bi} = 0$ the transport of an insoluble

surfactant and the corresponding Marangoni stress gives rise to an interior flow dominated by a clockwise circulation with a small toroidal flow around the pole as shown in figure 11(a). The corresponding tangential velocity is shown in figure 10(b). As the Biot number is increased to $\mathrm{Bi} = 10^{-2}$ the toroidal flow near the pole expands as shown in figure 11(b), with the corresponding tangential velocity in figure 10(b).

When we further increase the Biot number ($\mathrm{Bi} = 10$), the flow transitions to a counter-clockwise circulation with a small toroidal vorticity around the equator (figure 11(c)). The surfactant is more uniformly distributed (dash-dotted curve in figure 10(a) and the Marangoni stress is of the smallest magnitude in figure 10(c). This is because adsorption dominates in the surfactant kinetics, leading to a nearly uniform surfactant distribution on the drop surface and therefore smaller overall Marangoni stress at equilibrium. Results in

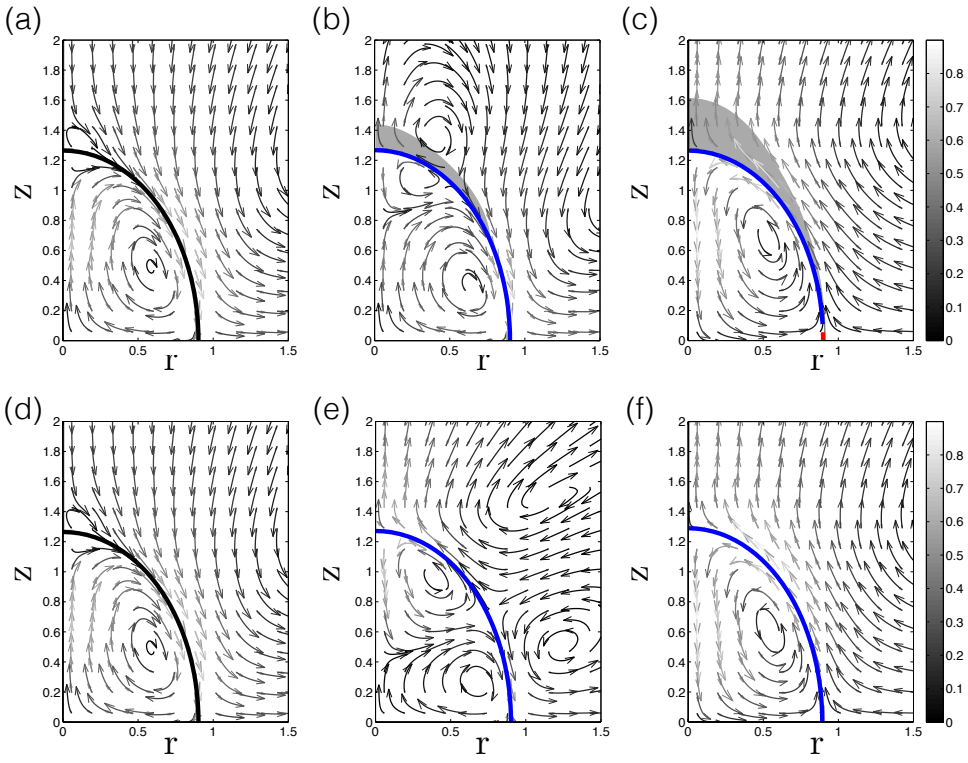

FIG. 11. Flow field for a prolate drop with $(\sigma_r, \varepsilon_r) = (1/3, 1)$ and $\mathrm{Ca}_E = 0.3$, corresponding to velocities in figures 10(b&e). (a) $\mathrm{Bi} = 0$; (b) $\mathrm{Bi} = 10^{-2}$ and $J = 2 \times 10^{-3}$; (c) $\mathrm{Bi} = 10$ and $J = 2 \times 10^{-3}$; (d) $\mathrm{Bi} = 0$; (e) $\mathrm{Bi} = 10^{-2}$ and $J = 10$; (f) $\mathrm{Bi} = 10$ and $J = 10$. The Péclet number $\mathrm{Pe} = \mathrm{Pe}_S = 500$.

figure 10 also show qualitative similarity in the effects of Bi between $J = 2 \times 10^{-3}$ (diffusion-controlled, figures 10(a-c)) and $J = 10$ (sorption-controlled, figures 10(d-f)).

Figure 11 compares the flow pattern between various values of Bi and J. The surface of the drop is color-coded to indicate adsorption (blue) and desorption (red). The grayscale colorbar indicates the change in bulk surfactants. For this prolate drop, adsorption dominates the kinetics and we expect the total surface surfactants to increase. This leads to a region depleted of bulk surfactant $C \approx 0.7$. For $J = 2 \times 10^{-2}$ our simulations show that adsorption takes place around the pole (figure 11(b)), and higher Biot number yields a wider surfactant-depleted region (figure 11(c)). Whereas increasing the transfer parameter to $J = 10$ does not change the qualitative features of the flow, the enhanced surfactant kinetics homogenizes the bulk surfactant. The toroidal flow is still observed at intermediate Biot numbers (figure 11(e)) however, it is now concentrated midway between the pole and equator.

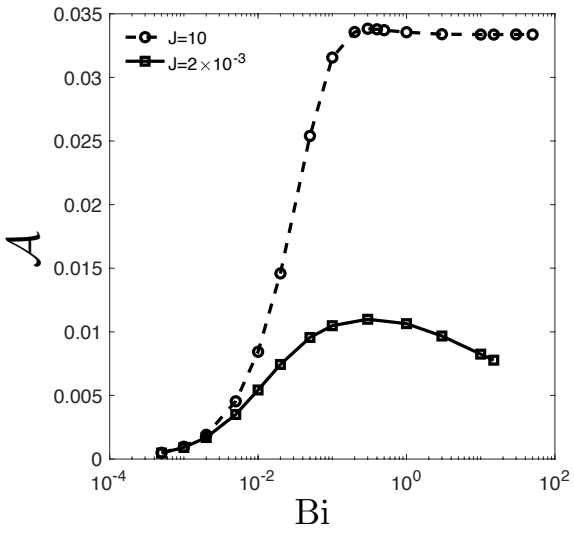

FIG. 12. Change in total amount $\mathcal{A}$ of surface surfactants for the prolate drop in §IV B with $(\sigma_r, \varepsilon_r) = (1/3, 1)$ and $\mathrm{Ca}_E = 0.3$. The Biot number $\mathrm{Bi} = 1$ and the Péclet number $\mathrm{Pe} = \mathrm{Pe}_S = 500$.

C. Effects of transfer parameter on total surface surfactant concentration and transient deformation dynamics

In this section we investigate how the total amount of surfactant on the drop surface depends on the transfer parameter J and Biot number Bi. We define $\mathcal{A}$ as the difference in

total amount of surfactant on the drop surface between time T and initial time 0:

$$\mathcal{A} \equiv \frac{1}{A_0}\left(A_T - A_0\right) \equiv \frac{1}{\int \Gamma(0)\ \mathrm{d}s}\left(\int \Gamma(T)\ \mathrm{d}s - \int \Gamma(0)\ \mathrm{d}s\right). \tag{17}$$

Using this definition, $\mathcal{A} > 0$ denotes adsorption, and $\mathcal{A} < 0$ represents desorption. At $T = 0$, the surfactant concentrations are uniformly applied in the respective domains, and $\mathcal{A} = 0$.

Figure 12 shows $\mathcal{A}$ as a function of Biot number, for the prolate drop in §IV B with an initially uniform surfactant distribution in the bulk. For $J = 2 \times 10^{-3}$ (solid curve), we see that $\mathcal{A}$ exhibits a non-monotonic behavior with a critical Biot number $\mathrm{Bi}_{\mathrm{cr}} \approx 0.3$, where the adsorbed surfactant concentration is maximized. Similarly for $J = 10$ (dashed curve) the difference in total surfactant reaches a maximum at a similar Biot number and then reaches a plateau.

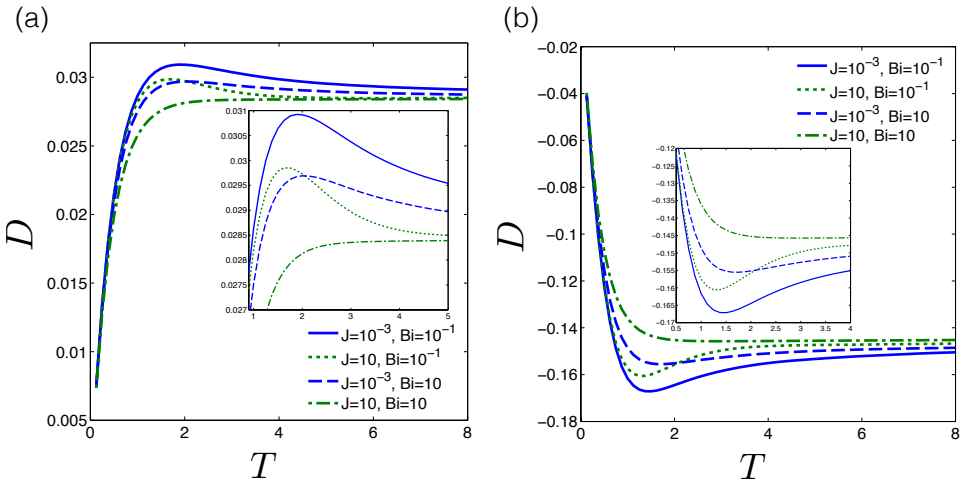

FIG. 13. Deformation as a function of dimensionless time T for (a) a prolate drop with $(\sigma_r, \varepsilon_r) = (0.97, 0.75)$, and (b) the oblate drop with $(\sigma_r, \varepsilon_r) = (4/3, 2)$. $\mathrm{Ca}_E = 0.25$ for both cases. The solid and dotted lines are for low ($J = 10^{-3}$), and high ($J = 10$) transfer parameter with $\mathrm{Bi} = 10^{-1}$, respectively. The dashed and dash-dotted lines represent higher Biot number ($\mathrm{Bi} = 10$) with $J = 10^{-3}$ and $J = 10$, respectively.

We also observe that the transient dynamics of drop deformation depends on J. For a prolate drop with $(\sigma_r, \varepsilon_r) = (0.97, 0.75)$ and a given value of Bi, figure 13(a) shows that the drop deformation number D displays an overshoot en route to the equilibrium for small J (the diffusion-controlled regime). Such overshoot in the drop deformation is found for weakly diffusive insoluble surfactant [45]. However, as shown in figure 13 (see inset for close-up of the transient overshoot), the transient overshoot dynamics is suppressed at large

J (the sorption-controlled regime). In this limit, the dynamics becomes closer to the uniform surface tension case [69] where the deformation monotonically reaches its equilibrium value. These observations also hold for oblate drops, as figure 13(b) illustrates for $(\sigma_r, \varepsilon_r) = (4/3, 2)$.

V. CONCLUSION

Experimental studies [55, 82–84] show that the transport of surface active agents (surfactants) is nonlinearly coupled with drop shape, adsorption/desorption kinetics, and hydrodynamic flow. Consequently analytical investigation on electrohydrodynamics of a viscous drop with surfactant sorption kinetics is challenging, and the numerical method in this study provides a tool to quantitatively investigate surfactant exchange between the bulk and the drop surface, and their effects on deformation. We show that surfactant solubility combines with the electric properties of the fluids in non-trivial ways to produce a wide range of electrohydrodynamics.

First we find that solubility affects the stability of a spheroidal drop by changing the balance between the capillary and electric pressures. Specifically we find that the surfactant solubility makes a prolate spheroidal drop lose instability if the total amount of surfactant increases (for $\sigma_r < 1$), while the prolate drop retains its stability when the total amount of surfactant increases (for $\sigma_r > 1$). Moreover, we show that solubility drastically changes the equilibrium flow: it suppresses multiple toroidal vortices that dominate in the absence of surfactant solubility. The resulting flow patterns resemble that observed for surfactant-free drops.

Second, we investigate the effects of the transfer parameter J. We find that increasing the transfer parameter J in the diffusion-controlled regime ($\mathrm{Bi}/J > 1$) pushes the drop hydrodynamics towards that of a clean drop by homogenizing the surfactant concentration on the drop surface. Under the same conditions, the average surface tension is also increased. As a result, deformation is suppressed for a given Ca_E as in the diffusion-controlled regime for a surfactant-laden bubble [69]. Similarly increasing the surfactant solubility $\mathrm{Bi} \geq 10$ homogenizes the surfactant distribution even more and the Marangoni stress is almost completely suppressed. Under these conditions the drop behaves as a clean drop with a much lower average surface tension, and transient overshoots in the deformation dynamics are no longer observed. We tested this hypothesis, and our numerical results show deformations

for the clean drop at $\gamma_{eq} = 0.54$ and surfactant-covered drop at large Bi and J are identical.

Further increase of J at a fixed Bi pushes the system into the sorption-controlled regime ($\mathrm{Bi}/J < 1$). In this regime the total amount of surfactant on the drop interface increases little and the average surface tension is not affected much by surfactant sorption kinetics. However, the spatial variation in surface surfactants is sufficient to induce different flow patterns for the range of electric capillary number we used in the simulations.

Our results suggest that the critical Ca_E for an equilibrium drop shape also depends on surfactant solubility. We are now investigating the correlation between the critical Ca_E and other parameters (such as the surfactant coverage χ and Bi), and how the various flow patterns develop at a stronger electric field strength.

ACKNOWLEDGEMENTS

HN acknowledges support from John J. and Char Kopchick College of Natural Sciences and Mathematics at Indiana University of Pennsylvania. WFH acknowledges support from Ministry of Science and Technology of Taiwan under research grant MOST-107-2115-M-005-004- MY2. MCL acknowledges support in part by Ministry of Science and Technology of Taiwan under research grant MOST-107-2115-M-009-016-MY3, and National Center for Theoretical Sciences. YNY acknowledges support from NSF under grant DMS-1614863, also support from Flatiron Institute, part of Simons Foundation.

---

[1] D. A. Saville, "Electrohydrodynamic stability: Fluid cylinders in longitudinal electric fields," Phys. Fluids **13**, 2987–2994 (1970).

[2] A. Ramos, H. Morgan, N. G. Green, and A. Castellanos, "Ac electrokinetics: a review of forces in microelectrode structures," J. Phys. D: Appl. Phys. **31**, 2338 (1998).

[3] A. Ramos, H. Morgan, N. G. Green, and A. Castellanos, "Ac electric-field-induced fluid flow in microelectrodes," J. Colloid Interface Sci. **217**, 420–422 (1999).

[4] A. Castellanos, A. Ramos, A. Gonzalez, N. G. Green, and H. Morgan, "Electrohydrodynamics and dielectrophoresis in microsystems: scaling laws," J. Phys. D: Appl. Phys. **36**, 2584–2597 (2003).

[5] M. Z. Bazant and T. M. Squires, "Induced-charge electrokinetic phenomena: Theory and microfluidic applications," Phys. Rev. Lett. **92**, 066101 (2004).

[6] O. D. Velev and K. H. Bhatt, "On-chip micromanipulation and assembly of colloidal particles by electric fields," Soft Matter **2**, 738 (2006).

[7] I. Hayati, A. I. Bailey, and T. F. Tadros, "Mechanism of stable jet formation in electrohydrodynamic atomization," Nature **319**, 41–43 (1986).

[8] A. Ramos and A. Castellanos, "Conical points in liquid-liquid interfaces subjected to electric fields," Phys. Lett. A **184**, 268–272 (1994).

[9] A. Ramos, H. Gonzalez, and A. Castellanos, "Experiments on dielectric liquid bridges subjected to axial electric fields," Phys. Fluids **6**, 3206–3208 (1994).

[10] D. A. Saville, "Electrohydrodynamic deformation of a particulate stream by a transverse electric field," Phys. Rev. Lett. **71**, 2907–2910 (1993).

[11] S. Torza, R. G. Cox, and S. G. Mason, "Electrohydrodynmaic deformation and burst of liquid drops," Proc. R. Soc. Lond. A **269**, 295–319 (1971).

[12] J. D. Sherwood, "Breakup of fluid droplets in electric and magnetic fields," J. Fluid Mech. **188**, 133–146 (1988).

[13] M. Trau, D. A. Saville, and I. A. Aksay, "Field-induced layering of colloidal crystals," Science **272**, 706–709 (1996).

[14] M. Trau, D. A. Saville, and I. A. Aksay, "Assembly of colloidal crystals at electrode interfaces," Langmuir **13**, 6375–6381 (1997).

[15] R. Vaidyanathan, S. Dey, L. G. Carrascosa, M. J. A. Shiddiky, and M. Trau, "Alternating current electrohydrodynamics in microsystems: Pushing biomolecules and cells around on surfaces," Biomicrofluidics **9**, 061501 (2015).

[16] Y. Mori and Y.-N. Young, "From electrodiffusion theory to the electrohydrodynamics of leaky dielectrics through the weak electrolyte limit," J. Fluid Mech. **855**, 67–130 (2018).

[17] C. T. O'Konski and H. C. Thacher, "The distortion of aerosol droplets by an electric field," J. Chem. Phys. **57**, 955–958 (1953).

[18] R. S. Allan and S. G. Mason, "Particle behaviour in shear and electric fields. I. Deformation and burst of fluid drops," Proc. R. Soc. Lond. A **267**, 45–61 (1962).

[19] Geoffrey Taylor, "Studies in electrohydrodynamics. I. the circulation produced in a drop by electric field," Proc. R. Soc. Lond. A **291**, 159–166 (1966).

[20] J. R. Melcher and G. I. Taylor, "Electrohydrodynamics: A review of the role of interfacial shear stresses," Annu. Rev. Fluid Mech. **1**, 111–146 (1969).

[21] J. A. Lanauze, L. M. Walker, and A. S. Khair, "The influence of inertia and charge relaxation on electrohydrodynamic drop deformation," Phys. Fluids **25**, 112101 (2013).

[22] J. A. Lanauze, L. M. Walker, and A. S. Khair, "Nonlinear electrohydrodynamics of slightly deformed oblate drops," J. Fluid Mech. **774**, 245 (2015).

[23] S. Mandal, A. Bandopadhyay, and S. Chakraborty, "Effect of surface charge convection and shape deformation on the dielectrophoretic motion of a liquid drop," Phys. Rev. E **93**, 043127 (2016).

[24] S. Mandal, A. Bandopadhyay, and S. Chakraborty, "The effect of surface charge convection and shape deformation on the settling velocity of drops in nonuniform electric field," Phys. Fluids **29**, 012101 (2017).

[25] D. Das and D. Saintillan, "A nonlinear small-deformation theory for transient droplet electrohydrodynamics," J. Fluid Mech. **810**, 225 (2017).

[26] N. Bentenitis and S. Krause, "Droplet deformation in DC electric fields: The extended leaky dielectric model," Langmuir **21**, 6194–6209 (2005).

[27] J. Zhang, J. D. Zahn, and H. Lin, "Transient solution for droplet deformation under electric fields," Phys. Rev. E **87**, 043008 (2013).

[28] M. Zabarankin, "A liquid spheroidal drop in a viscous incompressible fluid under a steady electric field," SIAM J. Appl. Math. **73**, 677–699 (2013).

[29] M. Zabarankin, "Analytical solution for spheroidal drop under axisymmetric linearized boundary conditions," SIAM J. Appl. Math. **76**, 1606–1632 (2016).

[30] P. R. Brazier-Smith, "Stability and shape of isolated and pairs of water drops in an electric field," Phys. Fluids **14**, 1 (1971).

[31] P. R. Brazier-Smith, S. G. Jennings, and J. Latham, "An investigation of the behaviour of drops and drop-pairs subjected to strong electric forces," Proc. R. Soc. Lond. A **325**, 363–376 (1971).

[32] M. Miksis, "Shape of a drop in an electric field," Phys. Fluids **24**, 1967 (1981).

[33] O. A. Basaran and L. E. Scriven, "Axisymmetric shapes and stability of charged drops in an external electric field," Phys. Fluids **1**, 799 (1989).

[34] G. Supeene, C. R. Koch, and S. Bhattacharjee, "Deformation of a droplet in an electric field: Nonlinear transient response in perfect and leaky dielectric mdeia," J. Colloid Int. Sci. **318**, 463–376 (2008).

[35] H. Nganguia, Y.-N. Young, A. T. Layton, W.-F. Hu, and M.-C. Lai, "An immersed interface method for axisymmetric electrohydrodynamic simulations in stokes flow," Commun. Comput. Phys. **18**, 429–449 (2015).

[36] W.-F. Hu, M.-C. Lai, and Y.-N. Young, "A hybrid immersed boundary and immersed interface method for electrohydrodynamic simulations," J. Comp. Phys. **282**, 47–61 (2014).

[37] D. A. Saville, "Electrohydrodynamics: The Taylor-Melcher leaky dielectric model," Annu. Rev. Fluid Mech. **29**, 27–64 (1997).

[38] J.-W. Ha and S.-M. Yang, "Deformation and breakup of Newtonian and non-Newtonian conducting drops in an electric field," J. Fluid Mech. **405**, 131–156 (2000).

[39] E. K. Zholkovskij, J. H. Masliyah, and J. Czarnecki, "An electrokinetic model of drop deformation in an electric field," J. Fluid Mech. **472**, 1–27 (2002).

[40] J.-W. Ha and S.-M. Yang, "Electrohydrodynamics and electrorotation of a drop with fluid less conducting than that of the ambient fluid," Phys. Fluids **12**, 764 (2000).

[41] E. Lac and G. M. Homsy, "Axisymmetric deformation and stability of a viscous drop in a steady electric field," J. Fluid Mech. **590**, 239 (2007).

[42] J.-W. Ha and S.-M. Yang, "Effects of surfactant on the deformation and stability of a drop in a viscous fluid in an electric field," J. Colloid Int. Sci. **175**, 369–385 (1995).

[43] K. E. Teigen and S. T. Munkejord, "Influence of surfactant on drop deformation in an electric field," Phys. Fluids **22**, 112104 (2010).

[44] H. Nganguia, Y.-N. Young, P. M. Vlahovska, J. Bławzdziewcz, J. Zhang, and H. Lin, "Equilibrium electro-deformation of a surfactant-laden viscous drop," Phys. Fluids **25**, 092106 (2013).

[45] H. Nganguia, O. S. Pak, and Y.-N. Young, "Effects of surfactant transport on electrodeformation of a viscous drop," Phys. Rev. E **99**, 063104 (2019).

[46] J. A. Lanauze, R. Sengupta, B. J. Bleier, B. A. Yezer, A. S. Khair, and L. M. Walker, "Colloidal stability dictates drop breakup under electric fields," Soft Matter **14**, 9351–9360 (2018).

[47] C. Sorgentone, A.-K. Tornberg, and P. Vlahovska, "A 3D boundary integral method for the electrohydrodynamics of surfactant-covered drops," J. Comput. Phys. **389**, 111–127 (2019).

[48] A. Poddar, S. Mandal, A. Bandopadhyay, and S. Chakraborty, "Sedimentation of a surfactant-laden drop under the influence of an electric field," J. Fluid Mech. **849**, 277–311 (2018).

[49] A. Poddar, S. Mandal, A. Bandopadhyay, and S. Chakraborty, "Electrical switching of a surfactant coated drop in poiseuille flow," J. Fluid Mech. **870**, 27–66 (2019).

[50] A. Poddar, S. Mandal, A. Bandopadhyay, and S. Chakraborty, "Electrorheology of a dilute emulsion of surfactant-covered drops," J. Fluid Mech. **881**, 524–550 (2019).

[51] S. Mandal, A. Bandopadhyay, and S. Chakraborty, "Dielectrophoresis of a surfactant-laden viscous drop," Phys. Fluids **28**, 062006 (2016).

[52] M. Ouriemi and P. M. Vlahovska, "Electrohydrodynamics of particle-covered drops," J. Fluid Mech. **751**, 106–120 (2014).

[53] L. Zhang, L. He, M. Ghadiri, and A. Hassanpour, "Effect of surfactants on the deformation and break-up of an aqueous drop in oils under high electric field strengths," J. Pet. Sci. Eng. **125**, 38–47 (2015).

[54] X. Luo, X. Huang, H. Yan, D. Yang, J. Wang, and L. He, "Breakup modes and criterion of droplet with surfactant under direct current electric field," Chem. Eng. Res. Des. **132**, 822–830 (2018).

[55] R. Sengupta, A. S. Khair, and L. M. Walker, "Electric fields enable tunable surfactant transport to micro scale fluid interfaces," Phys. Rev. E **100**, 023114 (2019).

[56] J. Chen and K. Stebe, "Marangoni retardation of the terminal velocity of a settling droplet: Role of surfactant physico-chemistry," J. Colloid Interface Sci. **178**, 144–155 (1996).

[57] C. D. Eggleton and K. J. Stebe, "An adsoprtion-desorption-controlled surfactant on a deforming droplet," J. Coll. Int. Sci. **208**, 68 (1998).

[58] J. Blawzdziewicz, E. Wajnryb, and M. Loewenberg, "Hydrodynamic interactions and collision efficiencies of spherical drops covered with an incompressible surfactant film," J. Fluid Mech. **395**, 29–59 (1999).

[59] E. K. Zholkovskij, V. I. Kovalchuk, S. S. Dukhin, and R. Miller, "Dynamics of rear stagnant cap formation at low reynolds numbers 1. slow sorption kinetics," J. Colloid Interface Sci. **226**, 51–59 (2000).

[60] W. J. Milliken and L. G. Leal, "The influence of surfactant on the deformation and breakup of a viscous drop: the effect of surfactant solubility," J. Coll. Int. Sci. **166**, 275–285 (1994).

[61] M. Hanyak, D. K. N. Sinz, and A. A. Darhuber, "Soluble surfactant spreading on spatially confined thin liquid films," Soft Matt. **8**, 7660 (2012).

[62] S. Le Roux, M. Roche, I. Cantat, and A. Saint-Jalmes, "Soluble surfactant spreading: How the amphiphilicity sets the marangoni hydrodynamics," Phys. Rev. E **93**, 013107 (2016).

[63] M. Sellier and S. Panda, "Unraveling surfactant transport on a thin liquid film," Wave Motion **70**, 183–194 (2017).

[64] U. Thiele, A. J. Archer, and L. M. Pismen, "Gradient dynamics models for liquid films with soluble surfactant," Phys. Rev. Fluids **1**, 083903 (2016).

[65] W. Li and N. R. Gupta, "Buoyancy-driven motion of bubbles in the presence of soluble surfactants in a newtonian fluid," Ind. Eng. Chem. Res. **58**, 7640–7649 (2019).

[66] D. Das and D. Saintillan, "Electrohydrodynamics of viscous drops in strong electric fields: numerical simulations," J. Fluid Mech. **829**, 127 (2017).

[67] S. L. Anna and H. C. Mayer, "Microscale tipstreaming in a microfluidic flow focusing device," Phys. Fluids **18**, 121512 (2006).

[68] C.-H. Chang and E. I. Franses, "Adsorption dynamics of surfactants at the air/water interface: a critical review of mathematical models, data and mechanisms," Colloids and Surfaces **100**, 1–45 (1995).

[69] Q. Wang, M. Siegel, and M. R. Booty, "Numerical simulation of drop and bubble dynamics with soluble surfactant," Phys. Fluids **26**, 052102 (2014).

[70] Y. Pawar and K. J. Stebe, "Marangoni effects on drop deformation in an extensional flow: The role of surfactant physical chemistry. I Insoluble surfactants," Phys. Fluids **8 (7)**, 1738–1751 (1996).

[71] D. E. Weidner, "Suppression and reversal of drop formation on horizontal cylinders due to surfactant convection," Phys. Fluids **25**, 082110 (2013).

[72] C. Kallendorf, A. Fath, M. Oberlack, and Y. Wang, "Exact solutions to the interfacial surfactant transport equation on a droplet in a Stokes flow regime," Phys. Fluids **27**, 082104 (2015).

[73] M. Muradoglu and G. Tryggvason, "A front-tracking method for computation of interfacial flows with soluble surfactants," J. Comp. Phys. **227**, 2238–2262 (2008).

[74] M.-C. Lai, C.-Y. Huang, and Y.-M. Huang, "Simulating the axisymmetric interfacial flows with insoluble surfactant by immersed boundary method," Int. J. Numer. Anal. Mod. **8**, 105–

117 (2011).

[75] J.-J. Xu, Y. Huang, M.-C. Lai, and Z. Li, "A coupled immersed interface and level set method for three-dimensional interfacial flows with insoluble surfactant," Commun. Comput. Phys. **15**, 451–469 (2014).

[76] J.-J. Xu, W. Shi, and M.-C. Lai, "A level set method for two-phase flows with soluble surfactant," J. Comput. Phys. **353**, 336–355 (2018).

[77] C. Sorgentone and A.-K. Tornberg, "A highly accurate boundary integral equation method for surfactant-laden drops in 3D," J. Comput. Physics **360**, 167–191 (2018).

[78] H. Nganguia, Y.-N. Young, A. T. Layton, M.-C. Lai, and W.-F. Hu, "Electrohydrodynamics of a viscous drop with inertia," Phys. Rev. E **93**, 053114 (2016).

[79] W.-F. Hu, M.-C. Lai, and C. Misbah, "A coupled immersed boundary and immersed interface method for interfacial flows with soluble surfactant," Comput. Fluids **168**, 201–215 (2018).

[80] J.-W. Ha and S.-M. Yang, "Effect of nonionic surfactant on the deformation and breakup of a drop in an electric field," J. Colloid Int. Sci. **206**, 195–204 (1998).

[81] P. F. Salipante and P. M. Vlahovska, "Electrohydrodynamics of drops in strong uniform dc electric fields," Phys. Fluids **22**, 112110 (2010).

[82] N. J. Alvarez, L. M. Walker, and S. L. Anna, "A microtensiometer to probe the effect of radius of curvature on surfactant transport to a spherical interface," Langmuir **26**, 13310–13319 (2010).

[83] N. J. Alvarez, W. Lee, L. M. Walker, and S. L. Anna, "The effect of alkane tail length of C_iE_8 surfactants on transport to the silicone oil-water interface," J. Colloid Interface Sci. **355**, 231–236 (2011).

[84] N. J. Alvarez, D. R. Vogus, L. M. Walker, and S. L. Anna, "Using bulk convection in a microtensiometer to approach kinetic-limited surfactant dynamics at fluid-fluid interfaces," J. Colloid Interface Sci. **372**, 183–191 (2012).

Appendix A: Numerical Implementation

We solve the governing equations in the axisymmetric cylindrical coordinates (r, z) (figure 14b), considering only the $r \geq 0$ half-plane. Once the solution is obtained, it is extended to the left half-plane by symmetry.

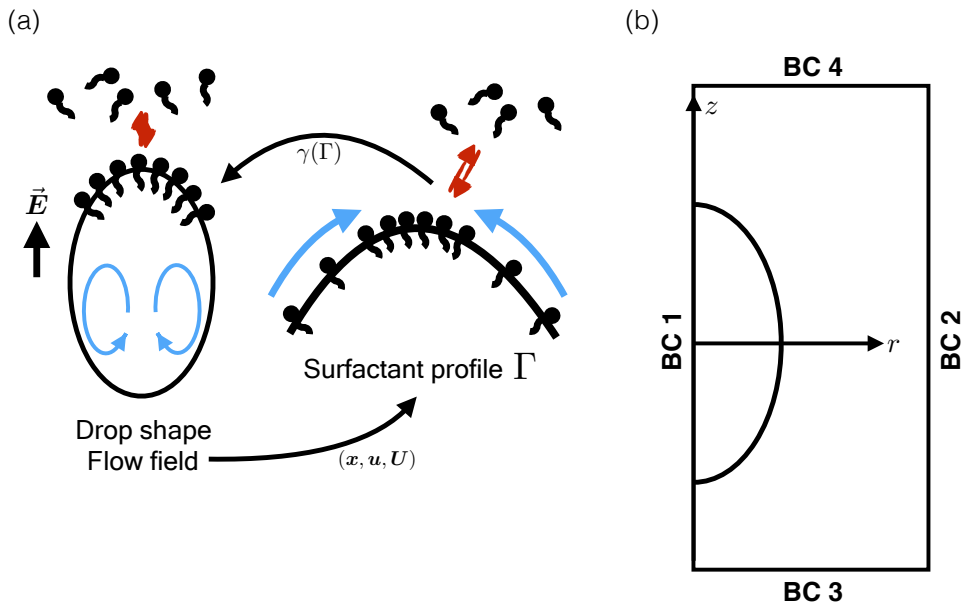

FIG. 14. (a) The numerical algorithm for the second-order immersed interface method code: At t_n the drop shape $\boldsymbol{x}$, flow field $\boldsymbol{u}$, and interface velocity, $\boldsymbol{U}$ are computed using the electrohydrodynamic solver in [35, 78]. The information is then used as input to the surfactant transport solver [79], in order to determine the bulk (ϕ) and interface surfactant profile (Γ). Given Γ, we determine the change in surface tension γ, as well as the updated drop shape, flow field, and interface velocity at time t_{n+1}. This process is repeated either until a steady-state is reached, or up to the onset of drop break-up. Flow circulation and direction are represented by the blue arrows. (b) Computational domain on the (r, z)-plane. On the walls BC 1, 2, 3, and 4 denote the boundary conditions (see text)

Figure 14a illustrates the algorithm. The droplet shape and position $\boldsymbol{x}$, flow field $\boldsymbol{u}$ and interface velocity $\boldsymbol{U}$ are computed using the IIM solver in [35, 78]. The boundary conditions in the computational domain $\Omega = [0, L] \times [-L, L]$ in figure 14b are given as follows: for the electric potential, $\phi^+ = \mp E_0 L/2$ at $z = \pm L$ (the bottom BC3 and top BC4 of the computational domain), while a Neumann boundary condition $\partial\phi/\partial r = 0$ is imposed on the sides $(r = 0,\ L)$ of the computational domain. For the Stokes equations, the pressure and velocity $\partial p/\partial r = 0$, $\partial w/\partial r = 0$, $u = 0$ at $r = 0$ (BC1), while Dirichlet boundary conditions are imposed on the other three sides (BC2-BC4) [35]. For the bulk surfactant concentration C, Neumann (BC1) and no flux (zero Neumann) (BC2-BC4) boundary conditions are imposed

[79]. Note that the soluble surfactant only exists outside of the drop.

For more detailed implementation steps and numerical methods, the reader is referred to [35] for the electrohydrodynamic solver. The three-dimensional axisymmetric soluble surfactant solver is a straightforward extension of the two-dimensional scheme in [79]. The main difference is in the treatment of the correction term for the curvature at the irregular grid nodes.

Appendix B: Validation

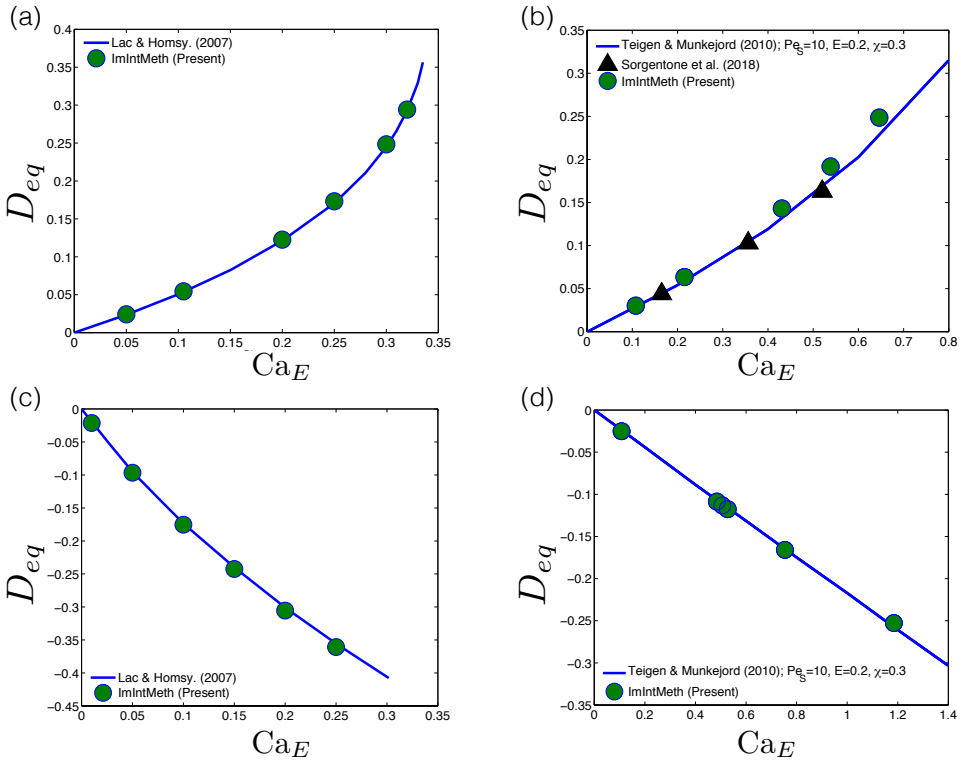

FIG. 15. Comparison between published simulation results for the clean drop case (a&c) in [41] and the surfactant-covered drop cases (b&d) in [43, 47]. The solid lines represent simulations from boundary integral for the clean case, and from level-set for the surfactant-covered drop case. The black triangles represent simulations from boundary integral, while the green circles represent simulations using the proposed immersed interface (IIM) implementation. For the clean drop cases: (a) $\sigma_r = 0.1,\ \varepsilon_r = 0.1$; (c) $\sigma_r = 0.5,\ \varepsilon_r = 20$. For the surfactant-covered drop cases we set $E = 0.2,\ \chi = 0.3,\ \mathrm{Pe}_s = 10,\ \mathrm{Bi} = 0$: (b) $\sigma_r = 0.3,\ \varepsilon_r = 1$; (d) $\sigma_r = 1,\ \varepsilon_r = 2$. Volume and total surfactant are conserved to within 5% in all cases.

We validate our numerical codes by comparing against results in the literature where the equilibrium deformation number D_{eq} is reported as a function of the electric capillary number Ca_E, for both a clean drop and and a drop laden with insoluble surfactant. L and B are the drop size along the major and minor axes, respectively. At moderate Ca_E, the equilibrium drop shape under a DC electric field could be either prolate or oblate. For an oblate drop, the circulation is always from the pole to the equator, while the flow inside a prolate drop can be either from the equator to the pole (prolate 'A') or from the pole to the equator (prolate 'B'). In our simulations the computational domain size is $[0, 5] \times [-5, 5]$. The step size $h = 5/N$ where $N = 256$, and the time step $\Delta t = h/10$.

Figure 15 shows comparisons for a clean drop (a&c) and for a surfactant-covered drop (b&d). We test our implementation against the boundary integral (BI) results from figures 5, and 19 in [41]. Figure 15a shows the equilibrium deformation number D_{eq} as a function of the capillary number Ca_E for a prolate drop with $\sigma_r = 0.1,\ \varepsilon_r = 0.1$, while the oblate drop is shown in figure 15c with $\sigma_r = 0.5,\ \varepsilon_r = 20$. These comparisons show good agreement with the present immersed interface method (IIM) results.

For the surfactant-covered drop, we consider the work in [43, 47] to validate the prolate and the oblate shapes. For these simulations, the electric parameters are set to $\sigma_r = 0.3,\ \varepsilon_r = 1$ for the prolate drop (case A in [43]), and $\sigma_r = 1,\ \varepsilon_r = 2$ for the oblate drop (case C in [43]). The elasticity constant $E = 0.2$ and the surfactant coverage $\chi = 0.3$. Other surfactant-related parameters are as follows: the surface and bulk Peclet numbers $\mathrm{Pe}_S = \mathrm{Pe} = 10$, respectively, and the Biot number $\mathrm{Bi} = 0$ (the insoluble surfactant limit). Figures 15b and 15d show excellent agreement between all three numerical methods: boundary integral (BI), immersed interface method (IIM), and regularized level-set method (RLSM).

Appendix C: Mesh refinement study

We perform a grid analysis (or mesh refinement) study. We consider a computational domain $\Omega = [0, 5] \times [-5, 5]$, to compute the L_∞ error and determine the ratio

$$\mathrm{Rate} = \frac{||A_N - A_{2N}||_\infty}{||A_{2N} - A_{4N}||_\infty}, \tag{C1}$$

where N is the grid size. The number of Lagrangian markers for the interface $M = N/2$. We run simulations to a final time $T = 0.5$ with time step $\Delta t = 10^{-3}$. The electric parameters

are $\mathrm{Ca}_E = 0.1$, $\varepsilon_r = 1$, $\sigma_r = 0.3$, corresponding to the prolate 'A' drop shape (case A in [43]). The surfactant parameters are $E = 0.2$, $\mathrm{Pe} = 10$, $\mathrm{Pe}_s = 10$, $\chi = 0.3$, and the solubility parameter $\mathrm{Bi} = 0.01$. Tables II-IV show the results of the analysis.

TABLE II. Numerical convergence for the flow field variables $\boldsymbol{u} = (u, v)$ and the pressure p.

N	$\|\|u_N - u_{2N}\|\|_\infty$	rate	$\|\|w_N - w_{2N}\|\|_\infty$	rate	$\|\|p_N - p_{2N}\|\|_\infty$	rate
32	1.769×10^{-1}	–	1.777×10^{-1}	–	7.303	–
64	2.724×10^{-2}	2.7	1.086×10^{-1}	0.711	5.408×10^{-2}	7.08
128	2.436×10^{-2}	0.161	4.21×10^{-2}	1.37	1.402×10^{-2}	1.95
256	2.498×10^{-3}	3.29	9.36×10^{-3}	2.17	2.025×10^{-3}	2.79

TABLE III. Numerical convergence for the component of interface markers $\boldsymbol{X} = (X, Y)$, the surface surfactant concentration Γ, the surface tension γ and surface tension gradient $\mathrm{d}\gamma$.

M	$\|\|\boldsymbol{X}_M - \boldsymbol{X}_{2M}\|\|_\infty$	rate	$\|\|\Gamma_M - \Gamma_{2M}\|\|_\infty$	rate
16	4.384×10^{-2}	–	1.053×10^{-1}	–
32	2.29×10^{-3}	4.29	9.954×10^{-3}	3.4
64	4.992×10^{-4}	2.17	1.72×10^{-3}	2.53
128	1.07×10^{-4}	2.2	5.522×10^{-4}	1.64
M	$\|\|\gamma_M - \gamma_{2M}\|\|_\infty$	rate	$\|\| \mathrm{d}\gamma_M - \mathrm{d}\gamma_{2M}\|\|_\infty$	rate
16	9.213×10^{-3}	–	2.27×10^{-3}	–
32	8.493×10^{-4}	3.44	1.223×10^{-3}	0.892
64	1.477×10^{-4}	2.52	2.897×10^{-4}	2.08
128	4.744×10^{-5}	1.64	4.765×10^{-5}	2.6

TABLE IV. Numerical convergence for the staggered variables: the electric potential (ϕ) and the bulk surfactant concentration (C).

N	$\|\|\phi_N - \phi_{2N}\|\|_\infty$	rate	$\|\|C_N - C_{2N}\|\|_\infty$	rate
32	1.556	–	2.016	–
64	4.179×10^{-1}	1.9	1.691	0.254
128	6.779×10^{-2}	2.62	1.451	0.221
256	1.035×10^{-2}	2.71	6.025×10^{-1}	1.27